



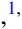



Compact inductor-capacitor resonators at sub-gigahertz frequencies

Qi-Ming Chen ^{1,*}, Priyank Singh,¹ Rostislav Duda ¹, Giacomo Catto,¹ Aarne Keränen,¹ Arman Alizadeh,¹ Timm Mörstedt,¹ Aashish Sah ¹, András Gunyhó ¹, Wei Liu ^{1,2} and Mikko Möttönen ^{1,3}

¹*QCD Labs, QTF Centre of Excellence, Department of Applied Physics, Aalto University, FI-00076 Aalto, Finland*

²*IQM Quantum Computers, Espoo 02150, Finland*

³*VTT Technical Research Centre of Finland Ltd. & QTF Centre of Excellence, P.O. Box 1000, 02044 VTT, Finland*



(Received 25 April 2023; revised 29 April 2023; accepted 19 October 2023; published 7 November 2023)

Compact inductor-capacitor (LC) resonators, in contrast to coplanar waveguide (CPW) resonators, have a simple lumped-element circuit representation but usually call for sophisticated finite-element method (FEM) simulations for an accurate modeling. Here we present a simple analytical model for a family of coplanar LC resonators where the electrical properties are directly obtained from the circuit geometry with a satisfying accuracy. Our experimental results on ten high-internal-quality-factor resonators ($Q_i \gtrsim 2 \times 10^5$), with frequencies ranging from 300 MHz to 1 GHz, show an excellent consistency with both the derived analytical model and detailed FEM simulations. These results showcase the ability to design sub-gigahertz resonators with less than 2% deviation in the resonance frequency, which has immediate applications, for example, in the implementation of ultrasensitive cryogenic detectors. The achieved compact resonator size of the order of a square millimeter indicates a feasible way to integrate hundreds of microwave resonators on a single chip for realizing photonic lattices.

DOI: [10.1103/PhysRevResearch.5.043126](https://doi.org/10.1103/PhysRevResearch.5.043126)

I. INTRODUCTION

Superconducting quantum circuits (SQC) provide a versatile platform of quantum engineering that has led to groundbreaking results in quantum-microwave communication [1–4], computation [5–9], simulation [10–18], and sensing [19–26]. Besides the celebrated Josephson effects, the rapid development of this field may be largely attributed to the wide application of coplanar waveguides (CPWs) [27–29], especially CPW resonators, which are ubiquitous throughout the SQC technology.

A CPW resonator is essentially a transmission line with short- or open-circuit boundary conditions. They can be modelled analytically, and are flexible in design and relatively simple to fabricate [29–31]. In SQC, the CPW resonators have a physical size comparable to or larger than the wavelength of the microwave field, $\lambda \approx 20$ mm at 5 GHz, making them particularly useful for circuits resonating in the microwave (1–100 GHz) regime. However, at sub-gigahertz frequencies, the relative permittivity of typical low-loss substrate materials, such as Si with $\epsilon_r \approx 11.9$, implies a CPW resonator to have a length of roughly 100 mm. Such a large structure shown in Fig. 1 (top) leads to severe limitations on the number of resonators that can be fit on a single chip. Winding the

waveguide into a spiral shape may be a convenient solution in certain cases [32–37], but it also raises new challenges such as impedance matching and grounding over such a long distance [38–41]. Other issues, such as coupling to the parasitic modes of the sample holder [42], should also be treated with extra care to design a huge structure.

An alternative, but less explored way for making superconducting resonators, is to use the lumped-element circuits such as the interdigital capacitors (IDCs) and meander-line inductors (MLIs). These circuits have a compact physical size being much smaller than the wavelength of the microwave field [43–50], as shown in Fig. 1 (bottom). The lumped-element inductor-capacitor (LC) resonators can be well described by a simple lumped-element parallel or series circuit consisting of an inductor L and a capacitor C . The mode volume is compact but the measured internal quality factor is still comparable to that of an CPW resonator [43]. Besides, the impedance is also easy to adjust in a large range, whereas that of a CPW resonator is normally upper bounded by approximately 377Ω [50]. However, estimating the precise values of L and C in a lumped-element resonator is generally challenging without using the finite-element method (FEM), which hinders their applications in SQC. The FEM simulations are especially resource-intensive for the lumped-element circuits, where the fine structures should be taken good care of with fine-enough mesh size. Furthermore, numerical results provide little intuition on how to adjust the geometry to obtain the desired values of L and C , respectively. Thus there is a great need in lumped-element-resonator design to estimate the electrical properties from the circuit geometry using convenient analytical equations, as explicitly called for in the recent studies of SQC [48,49].

*qiming.chen@aalto.fi

Published by the American Physical Society under the terms of the [Creative Commons Attribution 4.0 International](https://creativecommons.org/licenses/by/4.0/) license. Further distribution of this work must maintain attribution to the author(s) and the published article's title, journal citation, and DOI.

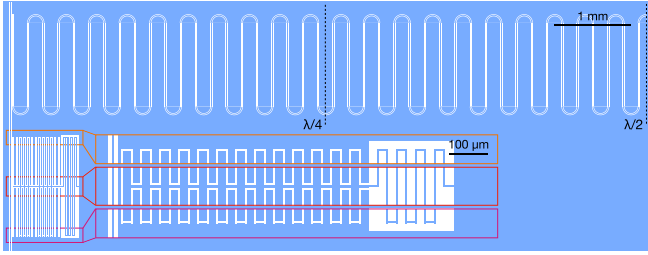


FIG. 1. Example of a CPW resonator (top) and a compact inductor-capacitor (LC) resonator (bottom) with a lowest resonance frequency of 1 GHz. Blue color indicates superconducting thin-film metal viewed from the top and white color denotes regions where the metal is etched away, exposing the substrate below the metal. Both resonators are coupled to a transmission line on the left of the structure. The width and gap (gap and width) of the capacitor (inductor) element in the LC resonator are chosen as 22 and 3 μm , respectively, for the ease of fabrication. The center-conductor width and gap of the CPW resonator are 10 and 6 μm , respectively, for achieving a 50- Ω characteristic impedance, yielding the total electrical length of 59 mm.

Although the values of L and C should be fully determined from the circuit layout, an accurate estimation of them is available only in simple cases. Fortunately, practical approximations for certain structures can already be found in the existing literature on microwave engineering [51–57]. It is therefore possible to model a compact LC resonator by synthesizing these early works in the specific context of SQC. In this study, we are particularly interested in the coplanar structures, such as MLIs and IDCs, as they are straightforwardly compatible with the thin-film technology used in SQC [51–57]. We first scrutinize the most useful design rules of MLIs and IDCs into compact analytical equations, and verify them in the typical parameter range of SQC via FEM. We then apply this knowledge to design sub-gigahertz LC resonators without FEM, with resonance frequencies ranging from 300 MHz to 1 GHz and impedances from 30 to 60 Ω . Subsequently, we implement the designs with one-step laser lithography and measure two samples at the cryogenic temperature of roughly 30 mK. Our experimental results show an excellent agreement with both the analytical model and the FEM simulations. These results provide a systematic study of compact LC resonators in SQC, and hence fill the sub-gigahertz frequency gap in the design of superconducting microwave resonators. The compact size and the high internal quality factor of the realized LC resonators is expected to advance the development of ultrasensitive microwave bolometers and calorimeters [22–26]. The achieved square-millimeter footprint also indicates a feasible way to build a large microwave resonator array on a single chip for quantum information processing and quantum simulations [58].

II. MEANDER-LINE INDUCTOR (MLI)

We consider a MLI which is made of a superconducting meandering wire. The current going through the wire creates a magnetic field that inhibits the change of the current itself,

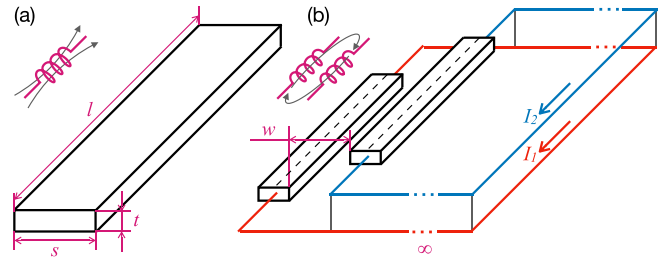


FIG. 2. Illustration of self and mutual inductances for a MLI. (a) The self-inductance of a single metal strip with width s , length l , and thickness t . (b) The mutual inductance between two parallel strips with a gap of w . Here, the circuit can be visualized as a solenoid which is formed by the parallel wires and the ground at an infinitely far distance. Depending on the direction of the currents flowing through the two wires, $I_1 = \pm I_2$, the mutual inductance can be either positive or negative.

corresponding to a self-inductance, L_s [Fig. 2(a)]. Because of the meander-line geometry, the magnetic fields generated by local parallel lines may also contribute to each other and lead to a mutual inductance, L_m [Fig. 2(b)]. We therefore describe the total inductance of the MLI element as

$$L = L_s + L_m. \quad (1)$$

The mutual inductance can be either positive or negative depending on the direction of current in the two parallel lines. The sign of L_m is determined by the so-called flux linkage, which is formally defined by an integral of the magnetic field over a Riemann surface bounded by the entire circuit. A simple visualization of the flux linkage is to imagine a returning current at an infinitely far distance, such that the two wires and the returning current forms a solenoid, as schematically shown in Fig. 2(b). The rule of thumb is to take the positive (negative) sign when the current in two parallel lines under consideration are pointing in the same (opposite) direction [52].

A. Self-inductance

In this section, we illustrate the self-inductance calculation with a simple geometry which leads to exact analytical solutions [51]. Here, a current I is flowing along the z axis in a cylindrical conductor of radius R and length l . The magnetic field at an arbitrary position \mathbf{r} in the xz plane outside the conductor can be calculated with the Biot-Savart law

$$\begin{aligned} \mathbf{B}(\mathbf{r}) &= \frac{\mu_0 I}{4\pi} \int_0^l \frac{d\hat{\mathbf{z}} \times (\mathbf{r} - \mathbf{z})}{|\mathbf{r} - \mathbf{z}|^3} \\ &= \frac{\mu_0 I}{4\pi} \left(\frac{l - z}{x\sqrt{x^2 + (l - z)^2}} + \frac{z}{x\sqrt{x^2 + z^2}} \right) \hat{\mathbf{y}}, \end{aligned} \quad (2)$$

where $\hat{\mathbf{x}}$, $\hat{\mathbf{y}}$, and $\hat{\mathbf{z}}$ are the orthonormal Cartesian unit vectors, and $\mu_0 = 4\pi \times 10^{-7}$ H/m is the permeability of free space. The magnetic flux penetrating the xz plane along the length of

the conductor is thus

$$\begin{aligned}\Phi_{\text{ext}} &= \int_R^\infty dx \int_0^l dz B(\mathbf{r}) \\ &= \frac{\mu_0 I}{2\pi} \left[l \ln \left(\frac{l + \sqrt{l^2 + R^2}}{R} \right) + R - \sqrt{l^2 + R^2} \right] \\ &\approx \frac{\mu_0 I l}{2\pi} \left[\ln \left(\frac{2l}{R} \right) - 1 \right],\end{aligned}\quad (3)$$

where we have assumed $l \gg R$ in the last row for simplification. This flux gives rise to the external part of the self-inductance

$$L_{\text{ext}} \approx \frac{\mu_0 l}{2\pi} \left[\ln \left(\frac{2l}{R} \right) - 1 \right]. \quad (4)$$

Inside the wire and under the low-frequency condition, we assume that the current is uniformly distributed over the cross section. This is valid for thin films where either the thickness t or the width s of the thin film is comparable to the London penetration depth, λ . The current that flows within a round-shaped cross section of radius x is thus $I x^2/R^2$. The fact that I flows in the z direction indicates that the magnetic field must be parallel to the xy plane, while the symmetry argument indicates that the field lines form circles centered at the z axis. In this regard, we simply apply Ampère's law and obtain

$$\mathbf{B}(x) = \frac{\mu_0 I x}{2\pi R^2} \hat{\mathbf{y}}. \quad (5)$$

We can therefore calculate the so-called flux linkage as

$$\Phi_{\text{int}} = \int_0^R dx \int_0^l dz \frac{x^2}{R^2} B(x) = \frac{\mu_0 I l}{8\pi}, \quad (6)$$

and therefore the internal part of the self-inductance

$$L_{\text{int}} = \frac{\mu_0 l}{8\pi}. \quad (7)$$

Here, the factor x^2/R^2 is introduced in the integral because the magnetic field created by the enclosed current, $I x^2/R^2$, does not occupy the entire cross section of the wire [51]. It is this factor that distinguishes the concept of flux linkage from the physical magnetic flux through a simple surface. These two concepts are equivalent to each other by introducing an appropriately chosen Riemann surface. In a N -turn solenoid, for example, such a Riemann surface is bounded by the winding wire, leading to the flux generated by a single turn to thread the circular cross section N times, thus enhancing the flux linkage. Here, we may visualize the factor, x^2/R^2 , as a fractional number of turns that the magnetic field penetrates the surface.

In total, we have the self-inductance of the wire as

$$L_s = L_{\text{int}} + L_{\text{ext}} \approx \frac{\mu_0 l}{2\pi} \left[\ln \left(\frac{2l}{R} \right) - \frac{3}{4} \right]. \quad (8)$$

We note that the above equation does not take the Meißner effect into consideration. A more detailed calculation of the internal part of the self-inductance and the kinetic inductance can be found in Appendix B.

We express the total self-inductance, L_s , in a slightly different form as

$$L_s = \frac{\mu_0 l}{2\pi} \left[\ln \left(\frac{2l}{r_{\text{GMD}}} \right) - 1 + \frac{r_{\text{AMD}}}{l} \right], \quad (9)$$

where $r_{\text{GMD}} = e^{-1/4} R$ and $r_{\text{AMD}} = R$ are the geometric and algebraic mean distances between all the points inside the cylinder wire, respectively [51,52]. We note that Eq. (8) can be recovered in the limit $R \ll l$. Conveniently, Eq. (10) may be generalized to conductors with an arbitrary cross section. In SQC, we are particularly interested in coplanar circuits compatible with thin-film technology. For a single metal strip of width s , length l , and thickness t , as shown in Fig. 2(a), we have $r_{\text{GMD}} \approx e^{-3/2}(s+t)$ and $r_{\text{AMD}} = (s+t)/3$ [51,52]. Thus we express the self-inductance as [52,53]

$$L_s \approx \frac{\mu_0 l}{2\pi} \left[\ln \left(\frac{2l}{s+t} \right) + \frac{1}{2} + \frac{s+t}{3l} \right]. \quad (10)$$

For zero-thickness thin film ($t \rightarrow 0$), we have

$$L_s \approx \frac{\mu_0 l}{2\pi} \left[\ln \left(\frac{2l}{s} \right) + \frac{1}{2} + \frac{s}{3l} \right]. \quad (11)$$

Assuming that $l/s > 2.23$, the reciprocal term in the above equation is 10 times smaller than the logarithmic term, and can be fairly neglected. Taking the partial derivative of L with respect to l and s , respectively,

$$\frac{\partial L_s}{\partial l} \approx \frac{\mu_0}{2\pi} \left[\ln \left(\frac{2l}{s} \right) + \frac{3}{2} \right], \quad (12)$$

$$\frac{\partial L_s}{\partial s} \approx -\frac{\mu_0 l}{2\pi s}, \quad (13)$$

we find that L_s is more sensitive to the changes in l than in s for $l/s < 3.42$.

B. Mutual inductance

In addition to self-inductance, currents flowing in parallel lines lead to mutual inductance. Here, we consider two parallel wires of equal length, l , which are separated by a gap of w . We define the pitch distance w_p as the distance between the centres of the two wires. The mutual inductance is given by [52,53]

$$L_m(l, w_p) = \pm \frac{\mu_0 l}{2\pi} Q(l, w_p), \quad (14)$$

where

$$\begin{aligned}Q(l, w_p) &= \ln \left[1 + \sqrt{1 + \left(\frac{w_{\text{GMD}}}{l} \right)^2} \right] - \ln \left(\frac{w_{\text{GMD}}}{l} \right) \\ &\quad + \left[\frac{w_{\text{GMD}}}{l} - \sqrt{1 + \left(\frac{w_{\text{GMD}}}{l} \right)^2} \right].\end{aligned}\quad (15)$$

Besides, w_{GMD} is the geometric mean distance of the two conductors, which can be well approximated as the pitch distance, $w_{\text{GMD}} \approx w_p$, in normal cases [53]. The positive (negative) sign is chosen if the current in the two lines are pointing in the same (opposite) direction [52]. We observe from the above equation that the absolute value of the mutual inductance, $|L_m|$, increases when decreasing w_{GMD} owing to the increase

of the flux linkage. Surprisingly, as pointed out by Ref. [53], the mutual inductance L_m does not depend on the conductor width s .

We note that the above results are valid for two identical parallel conductors with the same width s and length l , where $w_p = s + w$. For a more general case, where the two conductors have the same width, s , but different lengths, l_1 and l_2 , we have

$$2L_m(l_1, l_2, w_p) = L_m(l_2 + l_3, w_p) + L_m(l_1 - l_3, w_p) - L_m(l_3, w_p) - L_m(l_1 - l_2 - l_3, w_p). \quad (16)$$

Here, we have assumed that $l_1 \geq l_2$ and the end of the second conductor is shifted by l_3 compared with the first one. Another situation is that the two conductors have the same length l but different widths, s_1 and s_2 . A careful calculation of the geometric mean distance, w_{GMD} , indicates that [54]

$$\begin{aligned} \ln(w_{\text{GMD}}) = & \ln(w_p) - \frac{3}{2} \\ & + \frac{w_p^2}{2s_1s_2} \left[\left(1 + \frac{s_1 + s_2}{2w_p}\right)^2 \ln\left(1 + \frac{s_1 + s_2}{2w_p}\right) \right. \\ & + \left(1 - \frac{s_1 + s_2}{2w_p}\right)^2 \ln\left(1 - \frac{s_1 + s_2}{2w_p}\right) \\ & - \left(1 + \frac{s_1 - s_2}{2w_p}\right)^2 \ln\left(1 + \frac{s_1 - s_2}{2w_p}\right) \\ & \left. - \left(1 - \frac{s_1 - s_2}{2w_p}\right)^2 \ln\left(1 - \frac{s_1 - s_2}{2w_p}\right) \right]. \quad (17) \end{aligned}$$

When $s_1, s_2 \ll w_p$, the value of w_{GMD} depends only weakly on the widths of the two strips. It is thus convenient to replace w_{GMD} by w_p and neglect s in general when calculating mutual inductance.

C. Numerical results

To verify the applicability of the above equations in the typical parameter range of SQC, we numerically compare the analytical results with the FEM simulation for different control parameters. Here, we visualize a MLI as interdigital fingers made of the dielectrics, as indicated in Fig. 3, in order to keep the names of the variables consistent with the IDC that will be introduced in Sec. III. The definition of conductor width s , gap width w , and length l are consistent with those in Fig. 2. In addition, N denotes the number of the dielectric fingers. The self- and mutual inductances of the MLI can be estimated by combining Eqs. (11), (14), and (15). That is

$$L_s = NL_s(w + s) + (N + 1)L_s(l), \quad (18)$$

$$L_m = 2 \sum_{n=1}^N (N + 1 - n)L_m[l, n(w + s)]. \quad (19)$$

The factor of two in the mutual inductance originates from the summation over the distance between two arbitrary parallel lines. The total mutual inductance has a component caused by the current flowing in each of the two lines. Note that

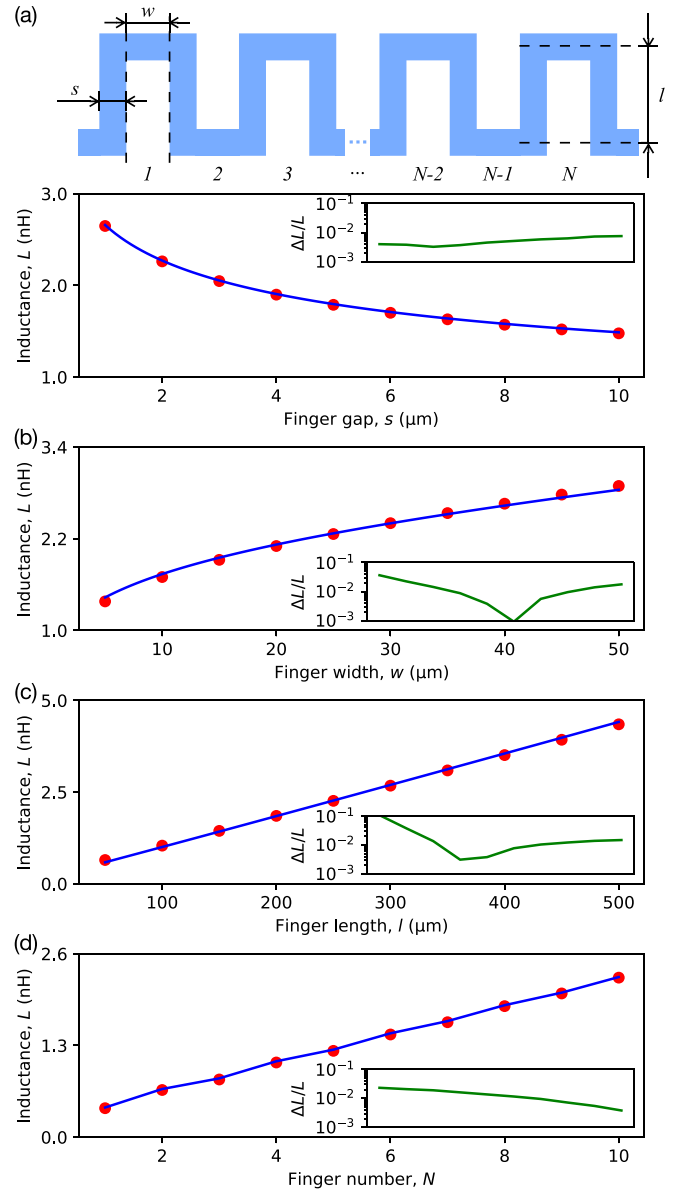


FIG. 3. Inductance L of a meander-line inductor (MLI) as a function of the (a) dielectric finger gap s (metallic wire width), (b) finger width w (wire gap), (c) length l , and (d) number N for the derived analytical equations (blue curves) and the FEM simulations (red dots). The insets show the relative difference between the analytical and FEM results. The parameter values of the MLI are $s = 2 \mu\text{m}$, $w = 25 \mu\text{m}$, $l = 250 \mu\text{m}$, and $N = 10$ unless given in the panel. The definitions of these parameters are illustrated in the top panel, with white color denoting the dielectrics and blue the conductor.

the sign of $L_m[l, n(w + s)]$ changes according to the relative orientations of the current, as indicated in Eq. (14). The total inductance is therefore readily obtained by adding the self- and mutual inductances according to Eq. (1).

The FEM simulations are carried out in Keysight advanced design system (ADS). Our tests on other software such as Sonnet and Ansys HFSS also provide similar results. Here, the Si substrate has a thickness of $675 \mu\text{m}$ and a relative permittivity of $\epsilon_r = 11.9$. The superconducting layer is assumed to be a perfect conductor with vanishing thickness. The mesh

TABLE I. Comparison of the computational time resources for FEM and the analytical results for the simulations in Figs. 3(a)–3(d).

s (μm)	1	2	3	4	5	6	7	8	9	10
FEM (s)	12	11	11	11	11	11	11	12	9	8
Anal. (μs)	31	24	23	23	23	24	23	23	24	23
w (μm)	5	10	15	20	25	30	35	40	45	50
FEM (s)	7	9	9	9	8	9	9	9	8	10
Anal. (μs)	36	27	26	26	30	27	25	25	25	25
l (μm)	50	100	150	200	250	300	350	400	450	500
FEM (s)	10	10	10	10	10	11	12	12	12	10
Anal. (μs)	34	25	25	25	25	25	24	25	25	25
N	1	2	3	4	5	6	7	8	9	10
FEM (s)	10	10	11	9	10	11	11	10	12	12
Anal. (μs)	15	8	10	15	14	23	19	20	23	24

is generated for 1 GHz frequency with 10^4 cells per wavelength. The mesh density at the edges are auto-determined by the Momentum engine of ADS. The inductance is evaluated at 100 MHz. We note that to define the ports for the FEM simulation, we have an extra $1 \mu\text{m}$ extension of the wire at the ends of the MLI.

Our numerical results are summarized in Fig. 3. We observe an excellent agreement between the analytical equations and the FEM results for all the chosen 40 sets of parameters. The average relative difference is at the level of 1%. The observed consistency thus demonstrates the correctness of the modeling of the MLI, where the electromagnetic parameters are directly obtained from the layout. In addition to the numerical consistency, we observe that the analytical approach shortens the simulation time by approximately six orders of magnitude, as shown in Table I. It indicates a dramatic improvement of the simulation efficiency that is important for the design of lumped-element circuits which involves optimization of their characteristic properties in a multidimensional parameter space, and hence a large number of solutions of the properties of the circuit.

We observe that the absolute value of the mutual inductance, L_m , is generally two times smaller than the self-inductance, L_s , in all the above simulations. It therefore indicates that a spiral layout of the superconducting wire may enhance the total inductance, L , by a factor of around 0.5, while a coplanar meandering-line layout suppresses L by 0.5 compared with the pure self-inductance. However, the major benefit of the meander-geometry is that it is easy to fabricate with the standard laser lithography tools in ordinary laboratory. Increasing the wire length may be the most effective way to improve the total inductance of the MLI.

III. INTERDIGITAL CAPACITOR (IDC)

The IDC is made of multiple superconducting thin films which interdigitate with each other like interleaved fingers [Fig. 4(a)]. The layout is dual to MLI if one swaps the conductor and the dielectric material. Here, we define two types of interior fingers with different widths, w_1 and w_2 , which are separated by a gap s . The width and the gap of the two exterior fingers are defined as w_E and s_E , respectively, as shown in Fig. 4(b). They may be different from those of the interior fingers. All fingers have the same length l and thickness t .

We neglect the two pads that connect the fingers with the feedlines, since they are spatially far away from each other and play a negligible role in general [57].

To derive analytical relations between the circuit geometry and the capacitance, C , we assume that $(N - 3)$ electrical walls with *zero* potential are located in the middle of each slot which are orthogonal to the sample plane [55]. Although this assumption can hardly be fulfilled in practical devices with a finite N , it is often valid when the slots are relatively narrow compared to the finger widths [56]. In this regard, we write the total capacitance of the IDC as

$$C = (N - 3) \frac{C_1 C_2}{C_1 + C_2} + 2C_E. \quad (20)$$

Here, C_1 and C_2 are the capacitances between interior fingers, i.e., type 1 and type 2 width different widths, and the electrical wall. We define C_E as the capacitance between the interior finger (Type 1) and the exterior finger in each unit cell [Fig. 4(b)].

Below, we assume zero-thickness metal strips ($t = 0$) to simplify the discussion. The finite-thickness case may be conveniently handled by resorting to Ref. [59], where we apply the so-called Wheeler's first order approximation and redefine

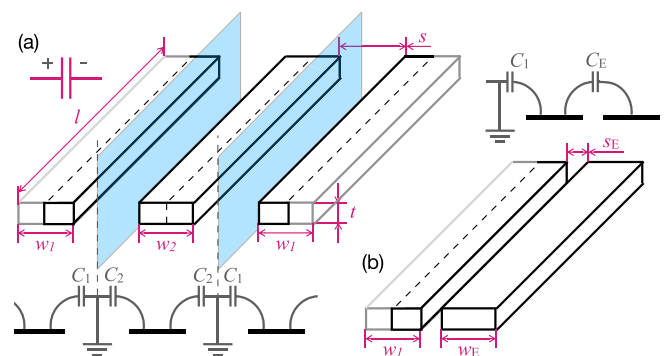


FIG. 4. Illustration of capacitance for an interdigital capacitor (IDC). (a) The capacitance between two adjacent interior fingers with length l , thickness t , and widths w_1 and w_2 , is calculated by summing over the capacitances, C_1 and C_2 , with respect to the electrical wall with *zero* potential in the center of the gap (gap size s). (b) The capacitance between the last interior finger and the exterior finger with width w_E is calculated directly without assuming an electrical wall in the middle of the gap (gap size s_E).

the finger width as

$$w' = w + \frac{t}{\pi} \left[1 + \ln \left(\frac{4\pi w}{t} \right) \right]. \quad (21)$$

A. Interior fingers

To calculate the capacitance, e.g., C_1 and C_2 , our major goal is to transform the coplanar geometry to an equivalent parallel plate geometry. The procedure is called conformal mapping, as detailed in Appendix A. We start from the Z domain where $z_1 = 0$, $z_2 = w_1/2$, $z_3 = w_1/2 + s/2$, and $z_4 = \infty$, rescale the first quadrant in the Z domain, apply the so-called Möbius and Schwarz–Christoffel transformations in sequence. This procedure transforms the original coplanar capacitor into a parallel plate capacitor with width $K(1/t_3)$, length l , and distance $K(\sqrt{1 - 1/t_3^2})$. Here, $K(\cdot)$ is the complete elliptic integral of the first kind and

$$t_3 = \frac{1}{\text{sn}[\eta_1 K(k_1), k_1]} \sqrt{\frac{1 - k_1^2 \text{sn}^2[\eta_1 K(k_1), k_1]}{1 - k_1^2}}. \quad (22)$$

with $\eta_1 = w/(w + s)$ being metallization ratio of the structure, and $\text{sn}(\cdot, k)$ the Jacobi elliptic function of modulus k . This result can be greatly simplified when assuming that the thickness of the substrate, h , is much larger than the width of the conductor, w_1 . That is

$$1/t_3 \approx \sin \left(\frac{\pi \eta_1}{2} \right), \quad (23)$$

The capacitance between the metal strip and the electrical wall through the upper half-plane in free space is thus

$$C_{1,0} = \epsilon_0 l \frac{K(1/t_3)}{K(\sqrt{1 - 1/t_3^2})}, \quad (24)$$

with $\epsilon_0 \approx 8.85 \times 10^{-12}$ F/m being the permittivity of free space. Similarly, the capacitance through the lower half-plane, which is filled with the substrate with dielectric constant ϵ_r , can be calculated as $C_{1,r} = \epsilon_r C_{1,0}$ [Fig. 7(f)]. In summary, the total capacitance of the unit cell (type 1) is

$$C_1 = 2\epsilon_{\text{eff}} C_{1,0}, \quad (25)$$

where $\epsilon_{\text{eff}} = (1 + \epsilon_r)/2$.

In the same way, one can calculate the total capacitance of the unit cell (type 2) as $C_2 = 2\epsilon_{\text{eff}} C_{2,0}$. Here, we have

$$1/t_3 \approx \sin \left(\frac{\pi \eta_2}{2} \right), \quad (26)$$

where $\eta_2 = w_2/(w_2 + s)$ and $h \gg w_2$. We note that we have neglected the edge effect when calculating the capacitance between two parallel plates. A more careful treatment requires the solution of the so-called Love equation, of which the analytical result with enough symmetry has been found only very recently [60,61].

B. Exterior fingers

One may follow the above procedure to derive C_E for the two cells with exterior fingers. Here, $C_E = C_1 C'_E / (C_1 + C'_E)$ with $C'_E = 2\epsilon_{\text{eff}} C'_{E,0}$, $C'_E = \epsilon_0 l K(1/t_3) / K(\sqrt{1 - 1/t_3^2})$, and $1/t_3 \approx \sin(\pi \eta_E/2)$. The metallization ratio is defined as $\eta_E = 2w_E/(2w_E + s)$. Strictly speaking, this formula is valid only for $w_E \simeq w_1, w_2$ [56]. However, it is found to be rather precise in the practice of microwave engineering [57].

For a more accurate result, we keep the last cell as a whole and define $z_1 = 0$, $z_2 = w_1/2$, $z_3 = w_1/2 + s_E$, $z_4 = w_1/2 + (s_E + w_E)$, and $z_5 = ih$ in the Z domain. The transformation

$$r = \sinh \left(\frac{\pi z}{2h} \right) \quad (27)$$

maps the points to the R domain and results in $r_5 = i$ and $r_1 = 0$ [57]. Following the transformations described above, we have

$$1/t_3 = \frac{\sinh[\pi w_1/(4h)]}{\sinh[\pi(w_1 + 2s_E)/(4h)]} \sqrt{\frac{\sinh^2[\pi(w_1 + 2s_E + 2w_E)/(4h)] - \sinh^2[\pi(w_1 + 2s_E)/(4h)]}{\sinh^2[\pi(w_1 + 2s_E + 2w_E)/(4h)] - \sinh^2[\pi w_1/(4h)]}}. \quad (28)$$

Finally, for $h \gg w_1, w_E$ we have

$$1/t_3 = \frac{w_1/2}{w_1/2 + s_E} \sqrt{\frac{(w_1/2 + s_E + w_E)^2 - (w_1/2 + s_E)^2}{(w_1/2 + s_E + w_E)^2 - (w_1/2)^2}}. \quad (29)$$

Correspondingly, we obtain $C_E = 2\epsilon_{\text{eff}} C_{E,0}$ and $C_{E,0} = \epsilon_0 l K(1/t_3) / K(\sqrt{1 - 1/t_3^2})$.

C. Numerical results

Similar to the study in MLI, we compare the analytical equations derived above with the numerical FEM results with different characteristic parameters, i.e., the finger number N , gap width s , and finger length l , and finger width w . The total capacitance can be estimated by combining Eqs. (20),

(A8), (A9), and (A10), where the metallization ratios for the three different unit cells are specified individually. The parameters s , w , l , and N are varied in ranges [1 μm , 10 μm], [5 μm , 50 μm], [50 μm , 500 μm], and [10,100]. To define the ports for the FEM simulation, we connect the fingers on each side by a 1 μm metal strip, which is 10 μm away from the end of the fingers on the other side. The comparison results are summarized in Fig. 5. The other parameters of the FEM solver are set as for the MLI in Sec. II C. Similar to the comparison of inductance simulations, the average relative difference is at the level of 1%. The excellent agreement between the analytical and the FEM results for all the chosen 40 geometries indicates the correctness of our modeling in this parameter range relevant for SQC. Moreover, the analytical approach shortens the simulation time by approximately six orders of magnitude, as shown in Table II. We note that the

TABLE II. Comparison of the computational time resources for FEM and the analytical results for the simulations in Figs. 5(a)–5(d).

s (μm)	1	2	3	4	5	6	7	8	9	10
FEM (s)	18	17	18	17	17	16	20	16	16	16
Anal. (μs)	127	51	53	50	49	49	50	53	53	50
w (μm)	5	10	15	20	25	30	35	40	45	50
FEM (s)	16	17	18	17	19	21	23	26	26	29
Anal. (μs)	119	52	52	53	50	50	50	51	50	55
l (μm)	50	100	150	200	250	300	350	400	450	500
FEM (s)	14	20	24	27	29	33	39	43	48	47
Anal. (μs)	149	59	59	59	59	58	59	58	58	58
N	10	20	30	40	50	60	70	80	90	100
FEM (s)	10	17	18	24	23	28	27	30	34	38
Anal. (μs)	121	56	52	51	50	50	50	49	49	49

efficiency of the FEM simulation depends highly on the size of the structures, whereas the efforts of the analytical approach remains unchanged. This favorable time scaling is particularly important to the design of sub-gigahertz lumped-element resonators, as we discuss in Sec. IV.

IV. COMPACT LC RESONATORS

With the above-derived knowledge of the MLI and the IDC, we connect them in parallel to design compact LC resonators without FEM. Here, we are particularly interested in the sub-gigahertz regime since it is not conveniently reachable by compact CPW resonators. The sub-gigahertz resonators also have an immediate application in superconducting thermal detectors, such as bolometers and calorimeters [22–26].

A. Experimental methods

We fabricate 10 compact LC resonators on two pure Si chips with an area of $10 \times 10 \text{ mm}^2$, denoted as sample A and B as showcased in Fig. 6(a). The sample substrate has a thickness of $675 \mu\text{m}$. A 200-nm-thick Nb layer is applied by sputtering, and then patterned by maskless laser lithography and reactive ion etching (RIE). The building block for the resonators in sample A are the MLI and IDC with the same parameter $s = 3 \mu\text{m}$, $w = 22 \mu\text{m}$, and $l = 1300 \mu\text{m}$. For sample B, we have $s = 2 \mu\text{m}$, $w = 18 \mu\text{m}$, and $l = 1200 \mu\text{m}$. In both cases, we adjust the number of these modules to reach the desired resonance frequency and impedance as close as possible. The relative permittivity of the substrate is chosen as $\epsilon_r = 11.9$ for design. The resonators are coupled to a common transmission line for multiplexed readout, such that each resonator forms a hanger-type geometry [62,63]. On each chip, the designed resonance frequencies increase from 300 MHz to 1 GHz separated by approximately 100 MHz. The designed impedances of the four low-frequency resonators decreases from 60Ω to 30Ω with the frequency, while they are kept below 30Ω for the four high-frequency resonators. However, we observe only five resonance peaks in each sample which we attribute to the possibly uneven RIE in the fabrication process.

We thermalize the samples at approximately 30 mK for characterization. The input line has approximately 60 dB of attenuation from room to cryogenic temperatures. We extract

the resonance frequency and the quality factors of each individual resonator from the transmission coefficients. In the vicinity of a single resonance frequency, we describe the measured transmission coefficient as [62,63]

$$S_{21}(\omega) = Ae^{-i(\omega\tau+\varphi)} \left(1 - \frac{e^{i\phi} Q_i/Q_e}{1 - i2Q_i\delta} \right), \quad (30)$$

where $\delta = (\omega - \omega_r)/\omega_r$, and ω_r is the resonance frequency that may be slightly different from the designed bare resonator frequency $\omega_0 = 1/\sqrt{LC}$ because of the coupling. The loaded, internal, and external quality factors are defined as Q_l , Q_e , and Q_i , respectively, which satisfy $1/Q_l = 1/Q_i + 1/Q_e$. The constant parameters A , τ , φ , and ϕ are related to the practical distortions to the measured spectrum. After correcting these distortions, the retrieved complex-valued spectrum forms a circle which is centered on the real axis and passes through a fixed point $(1 + i0)$ for $\omega \rightarrow \infty$. The radius of the circle is $Q_l/(2Q_e)$, while Q_l can be conveniently obtained by fitting the lineshape with a Lorentzian function.

B. Experimental results and analysis

Figures 6(b) and 6(c) summarize the measurement results. The excellent agreement between the designed and the extracted resonance frequencies indicates the accurate control of the resonance frequency [Fig. 6(b)] and therefore demonstrates the high accuracy of our analytical model consisting of the lumped-element components. On average over the 10 measured resonators, the experimentally obtained resonance frequency is 1.83% below the design frequency with a standard deviation of 1.44%. This small difference may have several possible origins such as the coupling between the resonator and the waveguide, which unavoidably shifts the actual resonance frequency from the designed value, $\omega_0/2\pi$, to a lower value. On the other hand, the previously neglected small contribution of the kinetic inductance also explains the observed systematic frequency drop. In addition, the small difference between the design and experiment can also arise from possible fabrication imperfections such as over etching of the Nb thin film during RIE.

Let us consider the effect of the coupling capacitance, C_{in} , between the transmission line and the lumped-element resonators on the resonance frequency. Take the design of sample B as an example. The $19 \mu\text{m}$ gap between the waveguide

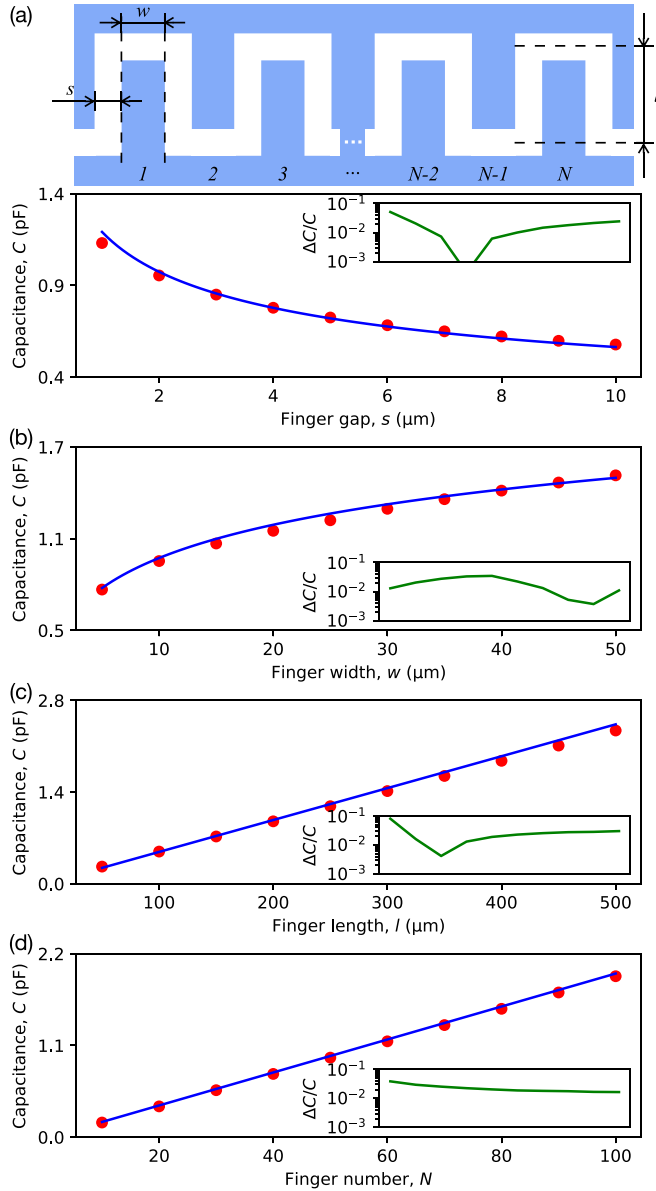


FIG. 5. Capacitance C of an interdigital capacitor (IDC) as a function of the (a) conductor finger gap s , (b) finger width w , (c) length l , and (d) number N for the analytical equations of the main text (blue curves) and the FEM simulations (red dots). The insets show the relative difference between the analytical and FEM results. The parameter values of the IDC are $s = 2 \mu\text{m}$, $w = 10 \mu\text{m}$, $l = 200 \mu\text{m}$, and $N = 50$ unless given in the panel. The definitions of these parameters are illustrated in the top panel, with white color denoting the dielectrics and blue the conductor.

and the resonators indicates a coupling capacitance at the ~ 100 fF scale, of which the exact value depends on the size of the IDCs. According to Ref. [62], the frequency shift of a hanger-type resonator can be approximately written as

$$\delta f = -Z_0 C_{\text{in}} \omega_0^2 / (\pi^2). \quad (31)$$

Here, Z_0 is the characteristic impedance of the resonator, which varies from 30 to 60 Ω in our case. Taking $C_{\text{in}} = 150$ fF and $Z_0 = 50 \Omega$ for all the resonators as a rough estimation, the mean deviation of the analytical and experimental results

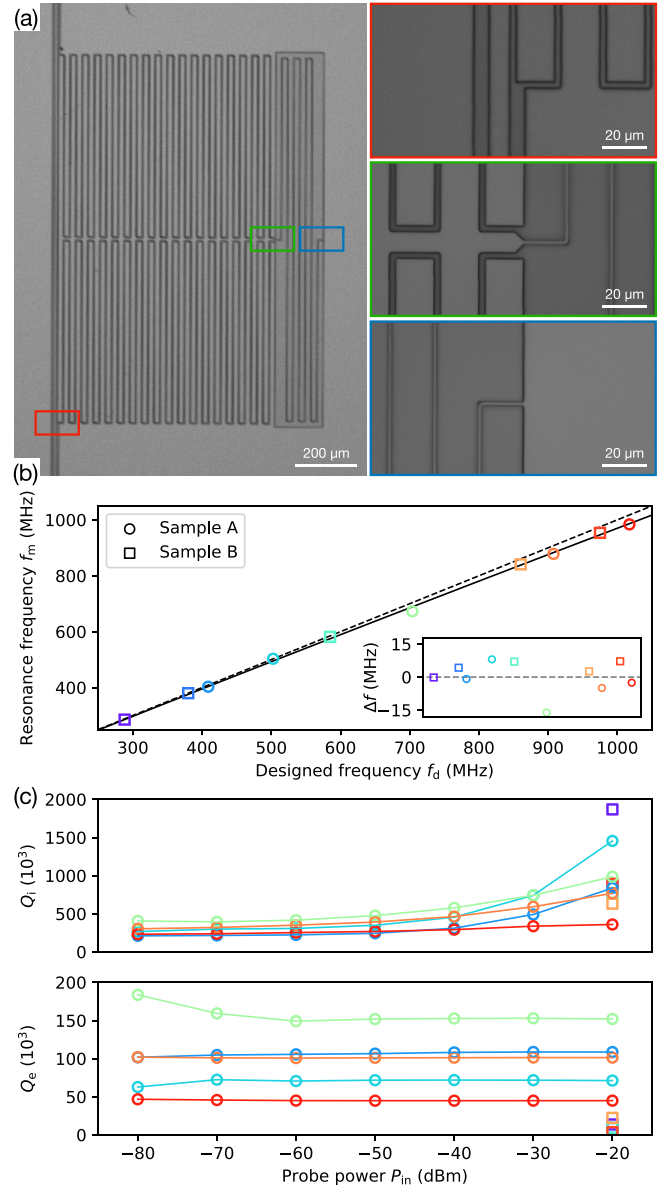


FIG. 6. Characterization results of the lumped LC resonators. (a) Optical photograph of one resonator in sample B with designed resonance frequency $\omega_0/2\pi = 600$ MHz. The insets show the enlarged area with higher resolution. The resonators in sample A have a ~ 5 times lower coupling strength to the waveguide by design. Here, the light color indicates Nb, and the dark color Si. (b) Comparison between the designed and measured resonance frequencies, f_d and f_m , respectively. The dashed line indicates the bare resonance frequencies without considering the coupling capacitance, C_{in} , while the solid line includes the coupling capacitance correction ($C_{\text{in}} = 150$ fF). The inset shows the difference between the measured resonance frequency and the designed frequency with coupling capacitance correction, $\Delta f = f_m - (f_d + \delta f)$. (c) Extracted values of the internal and external Q factors, Q_i and Q_e , under different probe power P_{in} . Here, the colors denote different resonators.

reduces significantly, to 0.84% with a standard deviation of 1.06%. Thus we may mostly attribute the systematic frequency drop of the real devices to the frequency shift induced by the coupling capacitor.

The extracted quality factors indicate a relatively long coherence time of the compact LC resonators [Fig. 6(c)]. At high probe power ($P_{\text{in}} = -20$ dBm at the room temperature), the average internal quality factor of all the 10 resonators is 944×10^3 with a standard deviation 405×10^3 . These values decrease with decreasing probe power but saturate at roughly -60 dBm. At the lowest probe power ($P_{\text{in}} = -80$ dBm), we obtain 283×10^3 and 69×10^3 for the mean internal quality factor and its standard deviation, respectively. We note that high-quality CPW resonators, in the 4–8 GHz range with $Q_i \geq 1000 \times 10^3$ at low probe power, can be routinely implemented. However, our achieved value of Q_i in the sub-gigahertz range has been seldom reached by CPW resonators. Moreover, our samples are fabricated in a single step without sophisticated techniques that are normally required for fabricating a high- Q CPW resonator, such as the wet-chemical post-processing approach for creating a clean and smooth interface between the thin film and air [64–68].

V. CONCLUSIONS

We provided a systematic study of meander-line inductors (MLIs) and interdigital capacitors (IDCs) in the context of superconducting quantum circuits (SQC), and combined them to design compact LC resonators at sub-gigahertz frequencies. The experimental results show an excellent agreement between the FEM simulations and the simple analytical equations provided in this study, where the resonance frequency was experimentally demonstrated with only about 2% deviation from the analytically obtained design value. These results promote the view that lumped-element inductors and capacitors can be accurately designed without resource-demanding FEM simulations. Consequently, these lumped-element resonators can be readily added to the toolkit of the SQC technology.

The physical size of a compact LC resonator is much smaller than the wavelength, which is in strong contrast to the CPW resonators. The usefulness of this compactness is pronounced at low frequencies where both the longitudinal and transverse dimensions can be tuned in a relatively large range below the wavelength. The feasibility of such a compact design is supported by the concept of photonic crystals, also referred to as metamaterials, where sub-wavelength structures are arranged periodically to tailor the behavior of the electromagnetic waves in a way that is beyond the capabilities of the uniform base material [69–71]. In our case, the unit cells are the 1300- μm -high 25- μm -wide patterns in the MLIs and IDCs.

The achieved compactness has a direct use in the current SQC technology. On one hand, fitting more circuit components on a single chip is a practical requirement when building large-scale quantum systems such as quantum computers or microwave photon lattices for quantum simulations [58]. The shown sub-gigahertz resonators already find important applications in cryogenic particle detection [22–26]. On the other hand, the sub-wavelength physical size confines the microwave photons in a small area which avoids the technical problem of keeping a precise impedance over an entire CPW resonator. The small mode volume naturally leads to a high and readily engineerable coupling strength to a nearby

device, such as a qubit [47,48]. The single-mode nature of lumped-element circuits also avoids the spurious effects of higher harmonics to the qubit lifetime and coherence, which is a known issue in SQC [72]. We may therefore expect a change of paradigm in circuit design for large-scale quantum information processing by combing the capabilities of compact LC resonators and superconducting qubits.

The PYTHON codes for generating and analyzing the data of this study are available online [73]

ACKNOWLEDGMENTS

This work is supported by the Academy of Finland Centre of Excellence program (No. 336810), European Research Council under Advanced Grant ConceptQ (No. 101053801), Business Finland Foundation through Quantum Technologies Industrial (QuTI) project (No. 41419/31/2020), Technology Industries of Finland Centennial Foundation, Jane and Aatos Erkkö Foundation through Future Makers program, Finnish Foundation for Technology Promotion (No. 8640), and Horizon Europe programme HORIZON-CL4-2022-QUANTUM-01-SGA via the Project No. 101113946 OpenSuperQPlus100. We thank Leif Grönberg for niobium deposition.

APPENDIX A: CONFORMAL MAPPING FOR CAPACITANCE CALCULATION

To calculate the capacitance, e.g., C_1 and C_2 , our major goal is to transform the coplanar geometry to an equivalent parallel plate geometry. The procedure is called conformal mapping, as illustrated in Figs. 7(a)–7(e). We start from the Z domain where $z_1 = 0$, $z_2 = w_1/2$, $z_3 = w_1/2 + s/2$, and $z_4 = \infty$ [Fig. 7(a)]. We rescale the first quadrant in the Z domain by a factor of $\alpha = K(k_1)/z_3$, such that $z'_1 = 0$, $z'_2 = \eta_1 K(k_1)$, $z'_3 = K(k_1)$, and $z'_4 = \infty$ [Fig. 7(b)], where we have named $\eta_1 = w/(w + s)$ as the so-called metallization ratio [56], $K(\cdot)$ is the complete elliptic integral of the first kind, and k_1 is an arbitrary constant to be determined. It is convenient to define

$$K(k_1)/K(k'_1) = (w + s)/(2h), \quad (\text{A1})$$

where $k'_1 = \sqrt{1 - k_1^2}$. It allows us to obtain a compact result when performing the following transformation from the Z domain to the R domain [Fig. 7(c)]

$$r = \text{sn}(z, k_1), \quad (\text{A2})$$

where $\text{sn}(\cdot, k)$ is the Jacobi elliptic function of modulus k . This transformation gives $r_1 = 0$, $r_2 = \text{sn}[\eta_1 K(k_1), k_1]$, $r_3 = 1$, and $r_4 = 1/k_1$.

Next, we apply the so-called Möbius transformation

$$t = \frac{r}{r_2} \sqrt{\frac{r_4^2 - r_2^2}{r_4^2 - r^2}}, \quad (\text{A3})$$

which transforms the first quadrant in the R domain to the first quadrant in the T domain with $t_1 = 0$, $t_2 = 1$, and $t_4 = \infty$ [Fig. 7(d)]. Besides, we have

$$t_3 = \frac{1}{\text{sn}[\eta_1 K(k_1), k_1]} \sqrt{\frac{1 - k_1^2 \text{sn}^2[\eta_1 K(k_1), k_1]}{1 - k_1^2}}. \quad (\text{A4})$$

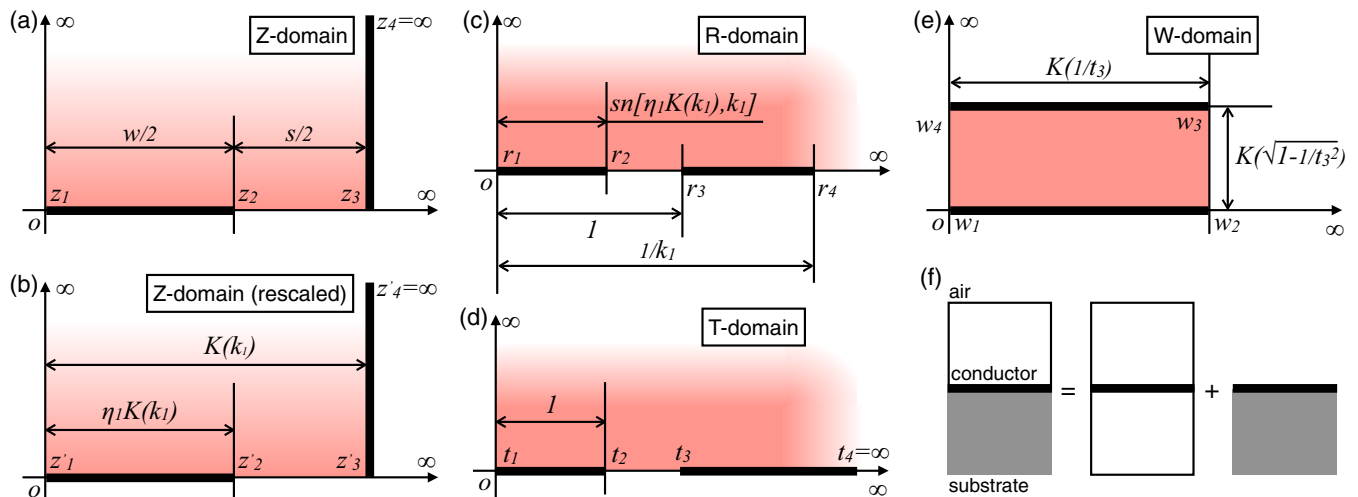


FIG. 7. [(a)–(e)] Sequence of conformal mappings that transforms the original problem into a problem of calculating the capacitance between two parallel plates. See text in Sec. A for details. (f) Configuration for partial capacitances for a thin-film conductor sandwiched between air and the substrate.

Finally, we apply the Schwarz–Christoffel mapping

$$w = \int_0^t dt' \frac{1}{\sqrt{(1-t'^2)[1-(t'/t_3)^2]}}, \quad (\text{A5})$$

which folds the first quadrant of the T domain into a rectangle in W domain with width, K , and height, K' [Fig. 7(e)]. In particular [74],

$$K = K(1/t_3) = \int_0^1 dt \frac{1}{\sqrt{(1-t^2)[1-(t/t_3)^2]}}, \quad (\text{A6})$$

$$K' = K(\sqrt{1-1/t_3^2}) = \int_1^{t_3} dt \frac{1}{\sqrt{(t^2-1)[1-(t/t_3)^2]}}, \quad (\text{A7})$$

where t_3 is defined in Eq. (A4). For $h \gg w_1$, we have $k_1 \rightarrow 0$ and $K(0) = \pi/2$ such that

$$1/t_3 = \sin\left(\frac{\pi\eta_1}{2}\right). \quad (\text{A8})$$

By applying the described sequence of conformal transformations, we transform the original coplanar capacitor into a parallel plate capacitor with width $K(1/t_3)$, length l , and distance $K(\sqrt{1-1/t_3^2})$. The capacitance between the metal strip and the electrical wall through the upper half-plane in free space is thus

$$C_{1,0} = \epsilon_0 l \frac{K(1/t_3)}{K(\sqrt{1-1/t_3^2})}, \quad (\text{A9})$$

with $\epsilon_0 \approx 8.85 \times 10^{-12}$ F/m being the permittivity of free space. Similarly, the capacitance through the lower half-plane, which is filled with the substrate with dielectric constant ϵ_r , can be calculated as $C_{1,r} = \epsilon_r C_{1,0}$ [Fig. 7(f)]. In summary, the total capacitance of the unit cell (type 1) is

$$C_1 = 2\epsilon_{\text{eff}} C_{1,0}, \quad (\text{A10})$$

where $\epsilon_{\text{eff}} = (1 + \epsilon_r)/2$.

APPENDIX B: KINETIC INDUCTANCE

Besides the geometric inductance discussed in Sec. II, superconducting thin films may carry a finite kinetic inductance. By definition, the energy stored in the kinetic inductance equals the kinetic energy of the charge carriers

$$\frac{1}{2} L_k I^2 = \int \frac{1}{2} m_s n_s v^2 dV, \quad (\text{B1})$$

where $m_s = 2m_e$ and n_s are the mass and density of Cooper pairs. Hence, $J_s = -2en_s v$ is the current density carried by Cooper pairs. At zero temperature, we may relate n_s to one half of the density of electrons contributing to conduction in the normal state of the material, i.e., $n_e/2$. With these definitions, we obtain the kinetic inductance as

$$L_k = \mu_0 \lambda^2 l \int J_s^2 dS / I^2, \quad (\text{B2})$$

where $\lambda = \sqrt{m_e / (\mu_0 n_e e^2)}$ is the London penetration depth.

Following Ref. [75], we express the magnetic field inside the thin film as

$$\mathbf{B}(x) \approx \frac{\mu_0 I}{2s} \frac{\sinh(x/\lambda)}{\sinh[t/(2\lambda)]} \hat{\mathbf{y}}. \quad (\text{B3})$$

Here, x varies from $-t/2$ to $t/2$, and the underlying assumption is that the width of the conductor, s , is much greater than its thickness, t . The current density is thus

$$\mathbf{J}_s(x) = \frac{I}{2\lambda s} \frac{\cosh(x/\lambda)}{\sinh[t/(2\lambda)]} \hat{\mathbf{z}}. \quad (\text{B4})$$

By combining Eqs. (B2) and (B4), we obtain for the kinetic inductance

$$L_k = \frac{\mu_0 \lambda l}{4s} \left[\coth\left(\frac{t}{2\lambda}\right) + \frac{(t/2\lambda)}{\sinh[t/(2\lambda)]} \right]. \quad (\text{B5})$$

In the thin-film limit ($t \ll \lambda$), we have $L_k = \mu_0 \lambda^2 l / (st)$. On the other hand, we have $L_k = \mu_0 \lambda l / (4s)$ in the thick-film limit ($t \gg \lambda$).

In fact, also the internal part of the self-inductance needs to be recalculated due to the non-uniform current redistribution

to be consistent with this level of approximation. Following the procedure presented in Sec. II A, we obtain [75]

$$L_{\text{int}} = \frac{\mu_0 \lambda l}{4s} \left[\coth\left(\frac{t}{2\lambda}\right) - \frac{(t/2\lambda)}{\sinh^2[t/(2\lambda)]} \right]. \quad (\text{B6})$$

It approaches $L_{\text{int}} = \mu_0 t l / (12s)$ and $L_{\text{int}} = \mu_0 \lambda l / (4s)$ in the thin- and thick-film limits, respectively. In comparison, a uniformly distributed current leads to an internal self-inductance of $L_{\text{int}} \approx \mu_0 t l / (6s)$ [76].

For simplicity, we denote the total internal inductance as the combination of the two parts, i.e.,

$$L'_{\text{int}} = \frac{\mu_0 \lambda l}{2s} \coth\left(\frac{t}{2\lambda}\right). \quad (\text{B7})$$

In typical superconductors such as Nb and Al, λ is below 50 nm. Assuming that the thickness of the thin film is $t = 200$ nm, the ratio between total internal inductance, L'_{int} , and the geometric self-inductance, L_s , calculated by Eq. (10) is approximately 5.1% at the lower limit of the above equation ($s = 200$ nm). This ratio decreases with s , and reaches 1.1% and 0.6% for $s = 1$ μm and $s = 2$ μm , respectively. This result indicates that the internal inductance, L'_{int} , may likely be neglected in the layout design if restricting the thin film to be wider than 1 μm . Note that this result does not apply to conductors where s is comparable or smaller than t . More detailed discussion of the kinetic inductance and its applications may be found elsewhere [77–81].

-
- [1] C. J. Axline, L. D. Burkhardt, W. Pfaff, M. Zhang, K. Chou, P. Campagne-Ibarcq, P. Reinhold, L. Frunzio, S. M. Girvin, L. Jiang, M. H. Devoret, and R. J. Schoelkopf, On-demand quantum state transfer and entanglement between remote microwave cavity memories, *Nat. Phys.* **14**, 705 (2018).
- [2] P. Kurpiers, P. Magnard, T. Walter, B. Royer, M. Pechal, J. Heinsoo, Y. Salathé, A. Akin, S. Storz, J.-C. Besse, S. Gasparinetti, A. Blais, and A. Wallraff, Deterministic quantum state transfer and remote entanglement using microwave photons, *Nature (London)* **558**, 264 (2018).
- [3] S. Pogorzalek, K. G. Fedorov, M. Xu, A. Parra-Rodriguez, M. Sanz, M. Fischer, E. Xie, K. Inomata, Y. Nakamura, E. Solano, A. Marx, F. Deppe, and R. Gross, Secure quantum remote state preparation of squeezed microwave states, *Nat. Commun.* **10**, 2604 (2019).
- [4] K. G. Fedorov, M. Renger, S. Pogorzalek, R. D. Candia, Q. Chen, Y. Nojiri, K. Inomata, Y. Nakamura, M. Partanen, A. Marx, R. Gross, and F. Deppe, Experimental quantum teleportation of propagating microwaves, *Sci. Adv.* **7**, eabk0891 (2021).
- [5] L. DiCarlo, J. M. Chow, J. M. Gambetta, L. S. Bishop, B. R. Johnson, D. I. Schuster, J. Majer, A. Blais, L. Frunzio, S. M. Girvin, and R. J. Schoelkopf, Demonstration of two-qubit algorithms with a superconducting quantum processor, *Nature (London)* **460**, 240 (2009).
- [6] E. Lucero, R. Barends, Y. Chen, J. Kelly, M. Mariantoni, A. Megrant, P. O'Malley, D. Sank, A. Vainsencher, J. Wenner, T. White, Y. Yin, A. N. Cleland, and J. M. Martinis, Computing prime factors with a josephson phase qubit quantum processor, *Nat. Phys.* **8**, 719 (2012).
- [7] Y. Zheng, C. Song, M.-C. Chen, B. Xia, W. Liu, Q. Guo, L. Zhang, D. Xu, H. Deng, K. Huang, Y. Wu, Z. Yan, D. Zheng, L. Lu, J.-W. Pan, H. Wang, C.-Y. Lu, and X. Zhu, Solving systems of linear equations with a superconducting quantum processor, *Phys. Rev. Lett.* **118**, 210504 (2017).
- [8] M.-C. Chen, M. Gong, X. Xu, X. Yuan, J.-W. Wang, C. Wang, C. Ying, J. Lin, Y. Xu, Y. Wu, S. Wang, H. Deng, F. Liang, C.-Z. Peng, S. C. Benjamin, X. Zhu, C.-Y. Lu, and J.-W. Pan, Demonstration of adiabatic variational quantum computing with a superconducting quantum coprocessor, *Phys. Rev. Lett.* **125**, 180501 (2020).
- [9] M. P. Harrigan, K. J. Sung, M. Neeley, K. J. Satzinger, F. Arute, K. Arya, J. Atalaya, J. C. Bardin, R. Barends, S. Boixo, M. Broughton, B. B. Buckley, D. A. Buell, B. Burkett, N. Bushnell, Y. Chen, Z. Chen, B. Chiaro, R. Collins, W. Courtney *et al.*, Quantum approximate optimization of non-planar graph problems on a planar superconducting processor, *Nat. Phys.* **17**, 332 (2021).
- [10] D. L. Underwood, W. E. Shanks, J. Koch, and A. A. Houck, Low-disorder microwave cavity lattices for quantum simulation with photons, *Phys. Rev. A* **86**, 023837 (2012).
- [11] A. A. Abdumalikov Jr, J. M. Fink, K. Juliusson, M. Pechal, S. Berger, A. Wallraff, and S. Filipp, Experimental realization of non-abelian non-adiabatic geometric gates, *Nature (London)* **496**, 482 (2013).
- [12] P. Roushan, C. Neill, A. Megrant, Y. Chen, R. Babbush, R. Barends, B. Campbell, Z. Chen, B. Chiaro, A. Dunsworth, A. Fowler, E. Jeffrey, J. Kelly, E. Lucero, J. Mutus, P. J. J. O'Malley, M. Neeley, C. Quintana, D. Sank, A. Vainsencher *et al.*, Chiral ground-state currents of interacting photons in a synthetic magnetic field, *Nat. Phys.* **13**, 146 (2017).
- [13] P. Roushan, C. Neill, J. Tangpanitanon, V. M. Bastidas, A. Megrant, R. Barends, Y. Chen, Z. Chen, B. Chiaro, A. Dunsworth, A. Fowler, B. Foxen, M. Giustina, E. Jeffrey, J. Kelly, E. Lucero, J. Mutus, M. Neeley, C. Quintana, D. Sank *et al.*, Spectroscopic signatures of localization with interacting photons in superconducting qubits, *Science* **358**, 1175 (2017).
- [14] A. J. Kollar, M. Fitzpatrick, and A. A. Houck, Hyperbolic lattices in circuit quantum electrodynamics, *Nature (London)* **571**, 45 (2019).
- [15] R. Ma, B. Saxberg, C. Owens, N. Leung, Y. Lu, J. Simon, and D. I. Schuster, A dissipatively stabilized mott insulator of photons, *Nature (London)* **566**, 51 (2019).
- [16] K. Xu, Z.-H. Sun, W. Liu, Y.-R. Zhang, H. Li, H. Dong, W. Ren, P. Zhang, F. Nori, D. Zheng, H. Fan, and H. Wang, Probing dynamical phase transitions with a superconducting quantum simulator, *Sci. Adv.* **6**, 25 (2020).
- [17] Q. Guo, C. Cheng, Z.-H. Sun, Z. Song, H. Li, Z. Wang, W. Ren, H. Dong, D. Zheng, Y.-R. Zhang, R. Mondaini, H. Fan, and H. Wang, Observation of energy-resolved many-body localization, *Nat. Phys.* **17**, 234 (2021).
- [18] Q.-M. Chen, M. Fischer, Y. Nojiri, M. Renger, E. Xie, M. Partanen, S. Pogorzalek, K. G. Fedorov, A. Marx, F. Deppe, and R. Gross, Quantum behavior of the duffing oscillator at the dissipative phase transition, *Nat. Commun.* **14**, 2896 (2023).

- [19] S. Barzanjeh, S. Pirandola, D. Vitali, and J. M. Fink, Microwave quantum illumination using a digital receiver, *Sci. Adv.* **6**, eabb0451 (2020).
- [20] A. Bienfait, P. Campagne-Ibarcq, A. H. Kiilerich, X. Zhou, S. Probst, J. J. Pla, T. Schenkel, D. Vion, D. Esteve, J. J. L. Morton, K. Moelmer, and P. Bertet, Magnetic resonance with squeezed microwaves, *Phys. Rev. X* **7**, 041011 (2017).
- [21] Z. Wang, M. Xu, X. Han, W. Fu, S. Puri, S. M. Girvin, H. X. Tang, S. Shankar, and M. H. Devoret, Quantum microwave radiometry with a superconducting qubit, *Phys. Rev. Lett.* **126**, 180501 (2021).
- [22] J. Govenius, R. E. Lake, K. Y. Tan, and M. Möttönen, Detection of zeptojoule microwave pulses using electrothermal feedback in proximity-induced josephson junctions, *Phys. Rev. Lett.* **117**, 030802 (2016).
- [23] R. Kokkonen, J. Govenius, V. Vesterinen, R. E. Lake, A. M. Gunyhó, K. Y. Tan, S. Simbierowicz, L. Grönberg, J. Lehtinen, M. Prunnila, J. Hassel, A. Lamminen, O.-P. Saira, and M. Möttönen, Nanobolometer with ultralow noise equivalent power, *Commun. Phys.* **2**, 124 (2019).
- [24] R. Kokkonen, J.-P. Girard, D. Hazra, A. Laitinen, J. Govenius, R. E. Lake, I. Sallinen, V. Vesterinen, M. Partanen, J. Y. Tan, K. W. Chan, K. Y. Tan, P. Hakonen, and M. Möttönen, Bolometer operating at the threshold for circuit quantum electrodynamics, *Nature (London)* **586**, 47 (2020).
- [25] S. Gasparinetti, K. L. Viisanen, O.-P. Saira, T. Faivre, M. Arzeo, M. Meschke, and J. P. Pekola, Fast electron thermometry for ultrasensitive calorimetric detection, *Phys. Rev. Appl.* **3**, 014007 (2015).
- [26] B. Karimi, F. Brange, P. Samuelsson, and J. P. Pekola, Reaching the ultimate energy resolution of a quantum detector, *Nat. Commun.* **11**, 367 (2020).
- [27] A. Wallraff, D. I. Schuster, A. Blais, L. Frunzio, R.-S. Huang, J. Majer, S. Kumar, S. M. Girvin, and R. J. Schoelkopf, Strong coupling of a single photon to a superconducting qubit using circuit quantum electrodynamics, *Nature (London)* **431**, 162 (2004).
- [28] J. Majer, J. M. Chow, J. M. Gambetta, J. Koch, B. R. Johnson, J. A. Schreier, L. Frunzio, D. I. Schuster, A. A. Houck, A. Wallraff, A. Blais, M. H. Devoret, S. M. Girvin, and R. J. Schoelkopf, Coupling superconducting qubits via a cavity bus, *Nature (London)* **449**, 443 (2007).
- [29] R. N. Simons, *Coplanar Waveguide Circuits, Components, and Systems* (John Wiley & Sons, New York, 2001).
- [30] L. Frunzio, A. Wallraff, D. Schuster, J. Majer, and R. Schoelkopf, Fabrication and characterization of superconducting circuit QED devices for quantum computation, *IEEE Trans. Appl. Supercond.* **15**, 860 (2005).
- [31] M. Göppl, A. Fragner, M. Baur, R. Bianchetti, S. Filipp, J. M. Fink, P. J. Leek, G. Puebla, L. Steffen, and A. Wallraff, Coplanar waveguide resonators for circuit quantum electrodynamics, *J. Appl. Phys.* **104**, 113904 (2008).
- [32] A. P. Zhuravel, C. Kurter, A. V. Ustinov, and S. M. Anlage, Unconventional rf photoresponse from a superconducting spiral resonator, *Phys. Rev. B* **85**, 134535 (2012).
- [33] N. Maleeva, M. V. Fistul, A. Karpov, A. P. Zhuravel, A. Averkin, P. Jung, and A. V. Ustinov, Electrodynamics of a ring-shaped spiral resonator, *J. Appl. Phys.* **115**, 064910 (2014).
- [34] N. Maleeva, A. Averkin, N. N. Abramov, M. V. Fistul, A. Karpov, A. P. Zhuravel, and A. V. Ustinov, Electrodynamics of planar archimedean spiral resonator, *J. Appl. Phys.* **118**, 033902 (2015).
- [35] M. Partanen, K. Y. Tan, J. Govenius, R. E. Lake, M. K. Mäkelä, T. Tantt, and M. Möttönen, Quantum-limited heat conduction over macroscopic distances, *Nat. Phys.* **12**, 460 (2016).
- [36] C. Rolland, A. Peugeot, S. Dambach, M. Westig, B. Kubala, Y. Mukharsky, C. Altimiras, H. le Sueur, P. Joyez, D. Vion, P. Roche, D. Esteve, J. Ankerhold, and F. Portier, Antibunched photons emitted by a dc-biased josephson junction, *Phys. Rev. Lett.* **122**, 186804 (2019).
- [37] C. Yan, J. Hassel, V. Vesterinen, J. Zhang, J. Ikonen, L. Grönberg, J. Goetz, and M. Möttönen, A low-noise on-chip coherent microwave source, *Nat. Electron.* **4**, 885 (2021).
- [38] J. Wenner, M. Neeley, R. C. Bialczak, M. Lenander, E. Lucero, A. D. O'Connell, D. Sank, H. Wang, M. Weides, A. N. Cleland, and J. M. Martinis, Wirebond crosstalk and cavity modes in large chip mounts for superconducting qubits, *Supercond. Sci. Technol.* **24**, 065001 (2011).
- [39] Y. J. Y. Lankwarden, A. Endo, J. J. A. Baselmans, and M. P. Bruijn, Development of NbTiN-al direct antenna coupled kinetic inductance detectors, *J. Low Temp. Phys.* **167**, 367 (2012).
- [40] M. Abuwasib, P. Krantz, and P. Delsing, Fabrication of large dimension aluminum air-bridges for superconducting quantum circuits, *J. Vac. Sci. Technol. B* **31**, 031601 (2013).
- [41] Z. Chen, A. Megrant, J. Kelly, R. Barends, J. Bochmann, Y. Chen, B. Chiaro, A. Dunsworth, E. Jeffrey, J. Y. Mutus, P. J. J. O'Malley, C. Neill, P. Roushan, D. Sank, A. Vainsencher, J. Wenner, T. C. White, A. N. Cleland, and J. M. Martinis, Fabrication and characterization of aluminum airbridges for superconducting microwave circuits, *Appl. Phys. Lett.* **104**, 052602 (2014).
- [42] M. Fischer, Q.-M. Chen, C. Besson, P. Eder, J. Goetz, S. Pogorzalek, M. Renger, E. Xie, M. J. Hartmann, K. G. Fedorov, A. Marx, F. Deppe, and R. Gross, In situ tunable nonlinearity and competing signal paths in coupled superconducting resonators, *Phys. Rev. B* **103**, 094515 (2021).
- [43] T. Lindström, J. E. Healey, M. S. Colclough, C. M. Muirhead, and A. Y. Tzalenchuk, Properties of superconducting planar resonators at millikelvin temperatures, *Phys. Rev. B* **80**, 132501 (2009).
- [44] H. G. Leduc, B. Bumble, P. K. Day, B. H. Eom, J. Gao, S. Golwala, B. A. Mazin, S. McHugh, A. Merrill, D. C. Moore, O. Noroozian, A. D. Turner, and J. Zmuidzinas, Titanium nitride films for ultrasensitive microresonator detectors, *Appl. Phys. Lett.* **97**, 102509 (2010).
- [45] M. S. Khalil, F. C. Wellstood, and K. D. Osborn, Loss dependence on geometry and applied power in superconducting coplanar resonators, *IEEE Trans. Appl. Supercond.* **21**, 879 (2011).
- [46] K. Geerlings, S. Shankar, E. Edwards, L. Frunzio, R. J. Schoelkopf, and M. H. Devoret, Improving the quality factor of microwave compact resonators by optimizing their geometrical parameters, *Appl. Phys. Lett.* **100**, 192601 (2012).
- [47] Z. Kim, B. Suri, V. Zaretsky, S. Novikov, K. D. Osborn, A. Mizel, F. C. Wellstood, and B. S. Palmer, Decoupling a cooper-pair box to enhance the lifetime to 0.2 ms, *Phys. Rev. Lett.* **106**, 120501 (2011).
- [48] D. C. McKay, R. Naik, P. Reinhold, L. S. Bishop, and D. I. Schuster, High-contrast qubit interactions using multimode cavity QED, *Phys. Rev. Lett.* **114**, 080501 (2015).

- [49] S. Weichselbaumer, P. Natzkin, C. W. Zollitsch, M. Weiler, R. Gross, and H. Huebl, Quantitative modeling of superconducting planar resonators for electron spin resonance, *Phys. Rev. Appl.* **12**, 024021 (2019).
- [50] M. Peruzzo, A. Trioni, F. Hassani, M. Zemlicka, and J. M. Fink, Surpassing the resistance quantum with a geometric superinductor, *Phys. Rev. Appl.* **14**, 044055 (2020).
- [51] F. W. Grover, *Inductance Calculations: Working Formulas and Tables* (Dover, New York, 1946).
- [52] H. Greenhouse, Design of planar rectangular microelectronic inductors, *IEEE Trans. Parts, Hybrids, Packag.* **10**, 101 (1974).
- [53] C. Yue and S. Wong, Physical modeling of spiral inductors on silicon, *IEEE Trans. Electron Devices* **47**, 560 (2000).
- [54] H.-M. Hsu, Analytical formula for inductance of metal of various widths in spiral inductors, *IEEE Trans. Electron Devices* **51**, 1343 (2004).
- [55] J. Wei, Distributed capacitance of planar electrodes in optic and acoustic surface wave devices, *IEEE J. Quantum Electron.* **13**, 152 (1977).
- [56] R. Igreja and C. Dias, Analytical evaluation of the interdigital electrodes capacitance for a multi-layered structure, *Sens. Actuator. A: Phys.* **112**, 291 (2004).
- [57] X. Bao, I. Ocket, J. Bao, Z. Liu, B. Puers, D. M. M.-P. Schreurs, and B. Nauwelaers, Modeling of coplanar interdigital capacitor for microwave microfluidic application, *IEEE Trans. Microwave Theory Tech.* **67**, 2674 (2019).
- [58] T. Ozawa, H. M. Price, A. Amo, N. Goldman, M. Hafezi, L. Lu, M. C. Rechtsman, D. Schuster, J. Simon, O. Zilberberg, and I. Carusotto, Topological photonics, *Rev. Mod. Phys.* **91**, 015006 (2019).
- [59] R. Esfandiari, D. Maki, and M. Siracusa, Design of interdigitated capacitors and their application to gallium arsenide monolithic filters, *IEEE Trans. Microwave Theory Tech.* **31**, 57 (1983).
- [60] E. R. Love, The electrostatic field of two equal circular co-axial conducting disks, *Q. J. Mech. Appl. Math.* **2**, 428 (1949).
- [61] B. Reichert and Z. Ristivojevic, Analytical results for the capacitance of a circular plate capacitor, *Phys. Rev. Res.* **2**, 013289 (2020).
- [62] Q.-M. Chen, M. Pfeiffer, M. Partanen, F. Fesquet, K. E. Honasoge, F. Kronowetter, Y. Nojiri, M. Renger, K. G. Fedorov, A. Marx, F. Deppe, and R. Gross, Scattering coefficients of superconducting microwave resonators. I. Transfer matrix approach, *Phys. Rev. B* **106**, 214505 (2022).
- [63] Q.-M. Chen, M. Partanen, F. Fesquet, K. E. Honasoge, F. Kronowetter, Y. Nojiri, M. Renger, K. G. Fedorov, A. Marx, F. Deppe, and R. Gross, Scattering coefficients of superconducting microwave resonators. II. System-bath approach, *Phys. Rev. B* **106**, 214506 (2022).
- [64] J. M. Martinis, K. B. Cooper, R. McDermott, M. Steffen, M. Ansmann, K. D. Osborn, K. Cicak, S. Oh, D. P. Pappas, R. W. Simmonds, and C. C. Yu, Decoherence in josephson qubits from dielectric loss, *Phys. Rev. Lett.* **95**, 210503 (2005).
- [65] J. Gao, M. Daal, A. Vayonakis, S. Kumar, J. Zmuidzinas, B. Sadoulet, B. A. Mazin, P. K. Day, and H. G. Leduc, Experimental evidence for a surface distribution of two-level systems in superconducting lithographed microwave resonators, *Appl. Phys. Lett.* **92**, 152505 (2008).
- [66] A. Romanenko and D. I. Schuster, Understanding quality factor degradation in superconducting niobium cavities at low microwave field amplitudes, *Phys. Rev. Lett.* **119**, 264801 (2017).
- [67] C. Müller, J. H. Cole, and J. Lisenfeld, Towards understanding two-level-systems in amorphous solids: insights from quantum circuits, *Rep. Prog. Phys.* **82**, 124501 (2019).
- [68] C. R. H. McRae, H. Wang, J. Gao, M. R. Vissers, T. Brecht, A. Dunsworth, D. P. Pappas, and J. Mutus, Materials loss measurements using superconducting microwave resonators, *Rev. Sci. Instrum.* **91**, 091101 (2020).
- [69] J. D. Joannopoulos, P. R. Villeneuve, and S. Fan, Photonic crystals: Putting a new twist on light, *Nature (London)* **386**, 143 (1997).
- [70] J. D. Joannopoulos, S. G. Johnson, J. N. Winn, and R. D. Meade, *Photonic Crystals: Molding the Flow of Light*, 2nd ed. (Princeton University Press, Princeton, 2008).
- [71] M. Skorobogatiy and J. Yang, *Fundamentals of Photonic Crystal Guiding* (Cambridge University Press, Cambridge, 2009).
- [72] A. A. Houck, J. A. Schreier, B. R. Johnson, J. M. Chow, J. Koch, J. M. Gambetta, D. I. Schuster, L. Frunzio, M. H. Devoret, S. M. Girvin, and R. J. Schoelkopf, Controlling the spontaneous emission of a superconducting transmon qubit, *Phys. Rev. Lett.* **101**, 080502 (2008).
- [73] <https://github.com/chenqmion/Lumped>.
- [74] M. Abramowitz and I. A. Stegun, *Handbook of Mathematical Functions with Formulas, Graphs, and Mathematical Tables* (US Government printing office, Washington, 1948), Vol. 55.
- [75] S. Doyle, P. Mauskopf, J. Naylor, A. Porch, and C. Duncombe, Lumped element kinetic inductance detectors, *J. Low Temp. Phys.* **151**, 530 (2008).
- [76] C. L. Holloway and E. F. Kuester, DC internal inductance for a conductor of rectangular cross section, *IEEE Trans. Electromagn. Compatibility* **51**, 338 (2009).
- [77] D. S. Hopkins, D. Pekker, P. M. Goldbart, and A. Bezryadin, Quantum interference device made by DNA templating of superconducting nanowires, *Science* **308**, 1762 (2005).
- [78] J. E. Mooij and Y. V. Nazarov, Superconducting nanowires as quantum phase-slip junctions, *Nat. Phys.* **2**, 169 (2006).
- [79] N. Samkharadze, A. Bruno, P. Scarlino, G. Zheng, D. P. DiVincenzo, L. DiCarlo, and L. M. K. Vandersypen, High-kinetic-inductance superconducting nanowire resonators for circuit QED in a magnetic field, *Phys. Rev. Appl.* **5**, 044004 (2016).
- [80] A. Murphy and A. Bezryadin, Asymmetric nanowire squid: Linear current-phase relation, stochastic switching, and symmetries, *Phys. Rev. B* **96**, 094507 (2017).
- [81] T. M. Hazard, A. Gyenis, A. Di Paolo, A. T. Asfaw, S. A. Lyon, A. Blais, and A. A. Houck, Nanowire superinductance fluxonium qubit, *Phys. Rev. Lett.* **122**, 010504 (2019).